

A COMPARATIVE STUDY OF WASP-67b AND HAT-P-38b FROM WFC3 DATA

GIOVANNI BRUNO¹, NIKOLE K. LEWIS, KEVIN B. STEVENSON, JOSEPH FILIPPAZZO, MATTHEW HILL, JONATHAN D. FRAINE,
HANNAH R. WAKEFORD

Space Telescope Science Institute, 3700 San Martin Drive, Baltimore, MD 21218, USA

DRAKE DEMING

Department of Astronomy, University of Maryland at College Park, College Park, MD 20742, USA

BRIAN KILPATRICK

Department of Physics, Box 1843, Brown University, Providence, RI 02904, USA

MICHAEL R. LINE

School of Earth & Space Exploration, Arizona State University, Phoenix, AZ 85282, USA

CAROLINE V. MORLEY

Department of Astronomy, Harvard University, Cambridge, MA 02138, USA

KAREN A. COLLINS

Department of Physics and Astronomy, Vanderbilt University, Nashville, TN 37235, USA

DENNIS M. CONTI

American Association of Variable Star Observers, 49 Bay State Rd., Cambridge, MA 02138 USA

JOSEPH GARLITZ

1155 Hartford St. Elgin, Oregon 97827 USA

JOSEPH E. RODRIGUEZ

Harvard-Smithsonian Center for Astrophysics, 60 Garden Street, Cambridge, MA 02138, USA

ABSTRACT

Atmospheric temperature and planetary gravity are thought to be the main parameters affecting cloud formation in giant exoplanet atmospheres. Recent attempts to understand cloud formation have explored wide regions of the equilibrium temperature-gravity parameter space. In this study, we instead compare the case of two giant planets with nearly identical equilibrium temperature ($T_{\text{eq}} \sim 1050$ K) and gravity ($g \sim 10$ m s⁻¹). During *HST* Cycle 23, we collected WFC3/G141 observations of the two planets, WASP-67 b and HAT-P-38 b. HAT-P-38 b, with mass 0.42 M_J and radius 1.4 R_{J} , exhibits a relatively clear atmosphere with a clear detection of water. We refine the orbital period of this planet with new observations, obtaining $P = 4.6403294 \pm 0.0000055$ d. WASP-67 b, with mass 0.27 M_J and radius 0.83 R_{J} , shows a more muted water absorption feature than that of HAT-P-38 b, indicating either a higher cloud deck in the atmosphere or a more metal-rich composition. The difference in the spectra supports the hypothesis that giant exoplanet atmospheres carry traces of their formation history. Future observations in the visible and mid-infrared are needed to probe the aerosol properties and constrain the evolutionary scenario of these planets.

Keywords: planets and satellites: atmospheres — planets and satellites: gaseous planets — planets and satellites: individual (WASP-67 b, HAT-P-38 b) — techniques: spectroscopic

1. INTRODUCTION

Exoplanet atmospheres are a unique window into the composition of exoplanets, their physical-chemical characteristics, and the interaction with their host stars. The degeneracy between aerosols and metallicity prevents from precisely constraining atmospheric composi-

tion (e.g. Deming et al. 2013; Wakeford & Sing 2015; Sing et al. 2016) and in particular the planetary mass-metallicity relation, a crucial piece of information in distinguishing among planet formation scenarios (e.g. Kreidberg et al. 2014a; Thorngren et al. 2016; Wakeford et al. 2017b).

Transmission spectroscopy is affected by condensates both in the visible and in the infrared. The WFC3/G141

¹ gbruno@stsci.edu

spectral band ($1.1 - 1.7 \mu\text{m}$) provides a number of examples of spectral features whose amplitude is muted with respect to models of clear atmospheres and solar composition (e.g. Deming et al. 2013; Kreidberg et al. 2014b; Wakeford & Sing 2015; Sing et al. 2016). One possible explanation for this is the intrinsic low water abundance of such atmospheres, with implications on their formation conditions (Seager et al. 2005; Madhusudhan et al. 2014a,b). However, Sing et al. (2016) present a comparative study of ten hot Jupiter atmospheres in both the visible and the infrared and provide evidence that clouds are the most likely explanation for the dampening of spectral features.

Aerosol formation is a strong function of the temperature, for which the equilibrium temperature T_{eq} is used as a proxy, of the gravity g of a planet, and of atmospheric composition. The giant planets characterized so far sit in a vast region of this phase space. They vary widely in temperature structure, which is determined by the radiative energy balance, and pressure structure of the atmosphere, mainly determined by the planet’s gravity. Despite this, the number of characterized exoplanets is still low, molecular abundances and pressure-temperature (P-T) profiles are in most cases poorly constrained, allowing only empirical trends to be tentatively identified (e.g. Stevenson 2016). Moreover, the population of characterized exoplanets lacks analyses of planets sharing similar parameters, which would enable testing whether models capture all the essential physics needed to correctly describe their aerosols.

In the context of comparative planetology, the pair of giant planets WASP-67 b and HAT-P-38 b is an interesting benchmark. Orbiting similar stars (early K and late G, respectively) with very similar metallicities (Hellier et al. 2012; Sato et al. 2012) at nearly equal orbital period (4.6 days), they share a similar level of insolation ($T_{\text{eq}} \sim 1050 \text{ K}$), unlike other planets in a similar region of the phase space. In addition, both planets are characterized by a gravity of about 10 m s^{-2} . They are therefore expected to have the same bulk properties, as well as to exhibit nearly identical P-T profiles, which we calculate with 1D atmosphere models (McKay et al. 1989; Marley et al. 1996; Fortney et al. 2008), assuming solar composition and cloud-free atmospheres. From the profiles and the condensation curves shown in Figure 1, we expect the planets to be in a regime where alkali elements condense (Lodders 1999; Burrows et al. 2000; Sudarsky et al. 2003; Fortney et al. 2003; Morley et al. 2012). Comparatively explaining aerosol formation in these two giant planets, sharing an almost equal amount of insolation as well as gravity, is an essential step towards understanding H_2 -He dominated atmospheres. Also, precise constraints on the molecular abundances of these planets would add a valuable contribution to our knowledge of the mass-metallicity relation and of planet formation.

In this work, we present a comparative analysis of the WFC3/G141 observations of WASP-67 b and HAT-P-38 b, collected during HST Cycle 23 (GO 14260, PI Deming). We introduce the targets in closer detail in Section 2 and Section 3 describes the observations. We present the fits of the observations to derive the planets’ transmission spectra in Section 4, while in Section 5 we interpret the spectra through retrieval exercises. We discuss and conclude in Section 7 and 8, respectively.

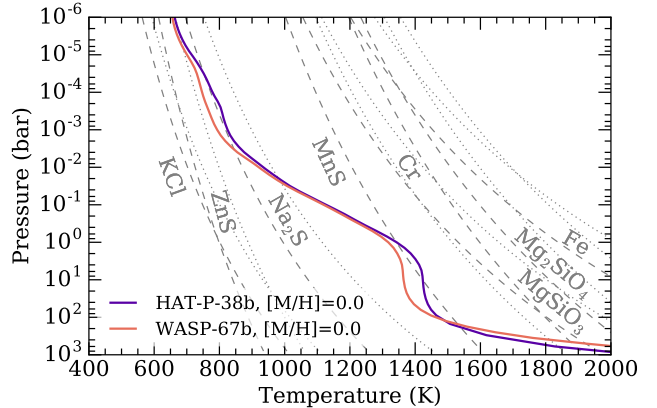


Figure 1. P-T profiles of the two planets from this work and condensation curves from various molecules. From the intersection of the curves, alkali-bearing condensates are expected in the atmospheres of the planets. WFC3 observations probe the pressures between about 1 and 100 mbars.

2. TARGETS

WASP-67 b (Hellier et al. 2012) orbits a 10.6 mag_J , $0.87 R_{\odot}$ K star ($T_{\text{eff}} = 5200 \pm 100$, $\log g = 4.35 \pm 0.15$, $[\text{Fe}/\text{H}] = -0.07 \pm 0.09$) with a 4.6-day orbital period. It is a $0.42 M_J$, $1.4 R_J$ inflated hot Jupiter with a grazing orbit (impact parameter $b > 0.9$). It is the first transiting exoplanet definitely known to have this characteristic. The grazing nature of its transit was confirmed by Mancini et al. (2014). This means the second and the third contact points are missing and causes the light curve solution to be degenerate. Mancini et al. (2014) carried out a multi-band follow-up of this system and found a flat spectrum within the experimental uncertainties, in agreement with the predictions of Fortney et al. (2008) for a planet of this temperature.

HAT-P-38 b (Sato et al. 2012), with mass $0.27 M_J$ and radius $0.83 R_J$, orbits a 11.0 mag_J , $0.92 R_{\odot}$, late G star ($T_{\text{eff}} = 5330 \pm 100$, $\log g = 4.45 \pm 0.08$, $[\text{Fe}/\text{H}] = 0.06 \pm 0.10$) with a period of 4.6 days. It is part of a rapidly increasing population of transiting Saturn-like planets with measured masses. At the time of writing, the `exoplanet.eu` archive contains 34 planets with $0.1 < M/M_J < 0.4$ and $0.7 < R/R_J < 1.1$, while only 14 of them were known at the time HAT-P-38 b was announced. The observed radius of this planet is slightly smaller than expected from the empirical relation of Enoch et al. (2011), who found a positive correlation between the radius of an exoplanet and its equilibrium temperature and a negative correlation between the radius and the metallicity of its host star. Following Fortney et al. (2007), Sato et al. (2012) suggest its peculiarity could be related to the heavy-element composition of its core. However, other members of the same family of exoplanets contradict such trend, such as HAT-P-18 b and HAT-P-19 b (Hartman et al. 2011) or Kepler-16AB b (Doyle et al. 2011).

3. OBSERVATIONS AND DATA REDUCTION

The WFC3 spectra of WASP-67 and HAT-P-38 are publicly available on the Mikulski Archive for Space Telescopes.² One visit of WASP-67 b was obtained on Oc-

² <https://archive.stsci.edu>

tober 22, 2016 (transit duration of 1.9 hours, requiring four *HST* orbits per transit), and two visits of HAT-P-38 b were secured on March 2, 2016 and on August 26, 2016 (transit duration of 3 hours, requiring five orbits per transit). The WASP-67 b data can be obtained at <https://doi.org/10.17909/T93D46> while the HAT-P-38 b data are at <https://doi.org/10.17909/T9768W>.

A direct image of the targets was obtained with the F139M filter at the beginning of each *HST* orbit. The spectra were acquired with the G141 grating, operating between 1.075 and 1.700 μm with a resolving power of 130 at 1.4 μm . Seventeen spectra per *HST* orbit were acquired for WASP-67 and thirteen per orbit for HAT-P-38. The spectra were acquired in spatial scanning mode (McCullough & MacKenty 2012), consisting in continuously nodding the telescope during the exposure. This allows for longer exposure times, therefore increasing the collected photons for bright targets and at the same time reducing overheads. Both targets were acquired in forward scanning direction only, with a scan rate of 0.037 arcsec s^{-1} (0.28 pixel s^{-1}) for WASP-67 b and of 0.026 arcsec s^{-1} (0.20 pixel s^{-1}) for HAT-P-38 b. We use the frames in IMA format, where non-destructive individual exposures, recorded every 22.3 seconds, are saved in separate *fits* extensions. Six non-destructive reads were obtained for each WASP-67 exposure, for a total exposure time of about 90 s, and eight for each HAT-P-38 exposure, for a total exposure time of about 134 s. The 256×256 pixels aperture was used in SPARS25 mode, yielding $\sim 34,000$ average electron counts per exposure for both targets. A first calibration of the raw images and correction for instrumental effects is carried out by the *calwf3* pipeline.

The wavelength calibration is derived by using the centroid of the direct image of the first orbit and by applying the relations in Pirzkal et al. (2016). We differentiate, mask, and add consecutive non-destructive reads (NDR) following Deming et al. (2013). The background subtraction is performed column-by-column, by selecting regions of the detector which are both above and below the stellar spectrum. A column-by-column 5σ clipping to reject cosmic rays and bad pixels is performed prior to the calculation of the column background median value. Figure 2 shows an example of background extraction for the first visit of HAT-P-38 b. The yellow boxes highlight the regions used for measuring the value of the background. For this visit in particular, we notice the presence of a contaminant source on the detector, which is clearly evident in the left part of the Figure. We also observe a residual charge in the central portion of the detector, which is less evident in the Figure. Our background correction and following extraction does not use the pixels affected by these effects. Each NDR is inspected for drifts both in the wavelength and in the scanning direction with the Python *image registration* package (Baker & Matthews 2001). Then, each NDR is integrated using the optimal extraction algorithm (Horne 1986) over an aperture determined by minimizing the residuals of the final white light curve from a transit model, as described in Section 4.1.

We obtain a set of one-dimensional spectra (one per NDR) which are added after correcting a second time for drifts in the wavelength direction which were not

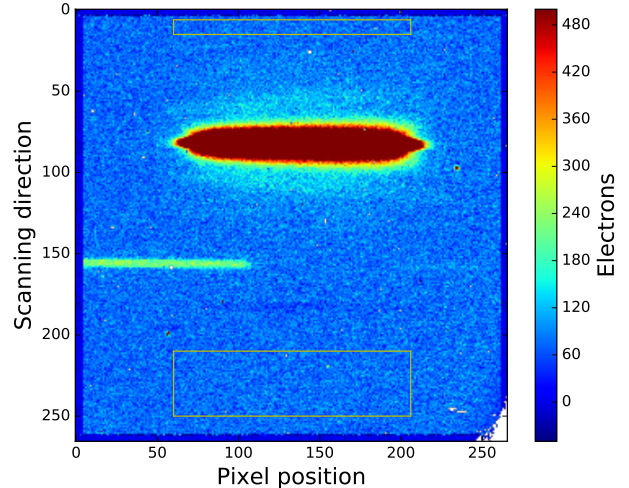


Figure 2. Background flux in a frame taken during the first visit of HAT-P-38 b. The x -axis shows the values of column pixel, prior to wavelength calibration. The yellow boxes indicate the regions used for background estimation. A contaminant source is evident in the left part of the frame, as well as a residual charge in the central columns, which we avoided in the estimation of the background value. Plotted measurements are limited in the range indicated in the right column.

corrected for in the previous phase, using a Fast Fourier Transform convolution algorithm to detect residual shifts. This is required because, even if *image registration* detects shifts in both directions of an image at the same time, the float precision it adopts can leave $\lesssim 0.1$ pixels shifts uncorrected. Figure 3 shows the spectrum after the extraction of one of the IMA files.

The integrated flux between 1.125 and 1.650 μm , in orange in the top panel of Figure 3, yields the photometric flux measurement corresponding to each point of the band-integrated, or “white”, light curves. Spectroscopic light curves are obtained by integrating the stellar spectra in channels, four to nine pixels (18.6 to 41.9 nm) wide. Repeating the transmission spectra extraction (Section 4.2) for various bin sizes allows us to assess the robustness of the reduction. While the bluemost wavelength used for the integration is kept fixed, different binnings produce ~ 10 nm different wavelengths for the redmost pixel. A slightly different band-integrated transit is therefore obtained for each binning. By minimizing the reduced χ^2 in the fit of such transits (section 4.1), we finally adopt a binning of seven pixels for WASP-67 b and of six pixels for HAT-P-38 b. However, the final interpretation is not affected by the choice of the bin size.

3.1. Ground-based observations

Additional transit observations were obtained by a group of advanced amateur astronomers that helped us constrain the orbital parameters of the systems. A full transit of WASP-67 b was observed using the Manner-Vanderbilt Ritchey-Chrétien (MVRC) telescope located at the Mt. Lemmon summit of Steward Observatory, AZ, on July 08, 2016 in the r' filter. The observations employed a 0.6 m f/8 RC Optical Systems Ritchey-Chrétien telescope and SBIG STX-16803 CCD with a $4\text{k} \times 4\text{k}$ array of 9 μm pixels, yielding a $26'.6 \times 26'.6$ field of view and $0''.39$ pixel $^{-1}$ image scale. The telescope was heavily defo-

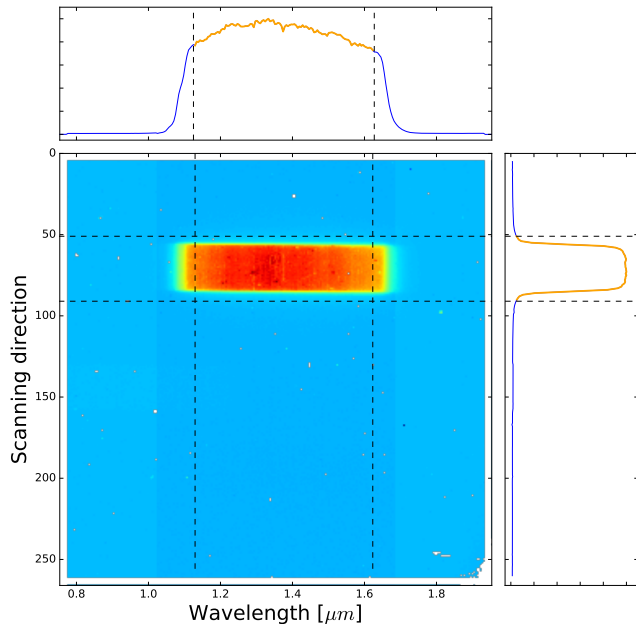


Figure 3. The 2D spectrum presented in Figure 2 after background subtraction and optimal extraction. On the top plot, the 1D spectrum after integration over the frame columns. On the right, the spectral trace in the cross-dispersion direction. The dashed lines and the orange color show the limits chosen for wavelength and aperture integration. The flux range goes from 0 to about 38000 electrons.

cused, resulting in a typical “donut” shaped stellar PSF with a FWHM of ~ 25 arcsec. The maximum elevation above the horizon of the observations was $\sim 35^\circ$. There were passing clouds at times, and data points corresponding to significant losses in atmospheric transparency have been removed from the data set.

The Garlitz Private Observatory (GPO) was used to observe a full transit of HAT-P-38 b on September 27, 2016. GPO is a private observatory run by Joseph Garlitz in Elgin, Oregon. The instrument consists of a 304.8 mm aperture Newtonian telescope with a focal length of 1505 mm, resulting in an f/4.9 focal ratio. The telescope uses an SBIG ST402me CCD camera resulting in a $15.5' \times 10.3'$ field of view and a $1.22''$ pixel scale. A clear filter was used with an exposure time of 60 seconds. 363 science images were taken at 60 seconds exposure each, with 21 images eliminated as outliers. FWHM was approximately 6.4 arcseconds. The differential photometry settings used were an aperture radius of 10 pixels, 18 pixels for the inner annulus radius, and 27 pixels for the outer annulus radius. Sky conditions were clear, temperature was 283 K, the moon was 8% waning, and image capture timing was synchronized using GPS.

We use the GPO observations of HAT-P-38 b to refine the ephemeris of the system, as discussed in the following Section.

4. TRANSIT MODELING

4.1. White light transits

Four *HST* orbits were required for the transit of WASP-67 b and five for each transit of HAT-P-38b. We follow the standard practice (e.g. Deming et al. 2013) of discarding the first *HST* orbit from each transit, which is affected by considerably different systematics than the

other ones. For the same reason, we also reject the first point of every orbit.

The band-integrated light curves are then modeled by combining a Mandel & Agol (2002) transit model, implemented in the `PyTransit` package (Parviainen 2015). The WFC3 systematics, i.e. planetary visit-long slope, *HST* breathing and “ramp” effect, are modeled with a combination of linear and exponential functions (e.g. Berta et al. 2012; Knutson et al. 2014; Kreidberg et al. 2014a,b; Fraine et al. 2014; Stevenson et al. 2014a; Wakeford et al. 2016; Kilpatrick et al. 2017). The fitted model is

$$M(t) = T(t, k_r, t_0, P, a/R_*, i, e, u_a, u_b) \times (C + V\theta + B\phi)(1 - \text{Re}^{-\psi/\tau}) \times F_b \quad (1)$$

where t is the time of the observation, k_r the planet-to-stellar radius ratio, t_0 the transit midpoint, P the orbital period, a/R_* the orbital semi-major axis normalized to the host star radius, i the orbital inclination, e the orbital eccentricity, u_a and u_b the linear and quadratic limb darkening coefficients. Because of the limited number of data points on the edges of the transits, we conservatively adopt a quadratic limb darkening law (Claret 2000): for our data sets, this does not produce appreciable differences in the fitted transit parameters with respect to more sophisticated limb darkening laws.

The parameter V accounts for a linear planetary visit-long trend, B for an *HST* orbit-long trend, and C is a vertical offset applied to the whole light curve. The ramp amplitude is modeled by the parameter R and its timescale by τ . The parameter F_b represents the baseline flux. The parameter ϕ is the *HST* orbital phase and θ is the planetary phase. The parameter ψ is instead the phase for the ramp feature, given by $2\pi[(t+t') \bmod P_{\text{HST}}]/P_{\text{HST}}$. The initial shift t' tracks the state of the ramp at the beginning of the observations. It is found by trial and error and is fixed to 0.025 for WASP-67 b and to 0.03 for HAT-P-38 b during the fit of the other parameters.

The Differential Evolution Markov Chains algorithm of the `MC3` package (Cubillos et al. 2016) is used to sample the posterior distributions of the model parameters. An initial Levenberg-Marquardt exploration is performed prior to the start of the chains and its result is used for the initial values of the jump parameters. We refer to the most updated papers (Hellier et al. 2012; Sato et al. 2012) for the ephemeris and orbital parameters of each system P , a/R_* , i , and e , listed in table 1. The parameters a/R_* and i are fixed, as the *HST* observations do not sample the transit profile edges. Their values are checked against a transit-only modeling performed with `PyTransit` and `MC3`, without systematics, of our MVRG and GPO observations. The corresponding transits and the respective best-fit models are shown in Figure A.17. We find agreement between the parameters a/R_* and i from the ground-based observations, indicated in Table 1. Despite the smaller uncertainties in our fits, the published values are conservatively adopted.

Because of the possible biases in our current knowledge of the radius distribution of planets, we consider the planet-to-stellar radius ratio (k_r) as a scale parameter and use a Jeffrey prior as suggested by Gregory (2005).

We instead use a uniform prior for the transit midpoint (t_0) jump parameter. The distributions for both k_r and t_0 are centered around the most recent values available from literature. For the purpose of the fit, the first point of each observation is set to 0 BJD. The limb darkening coefficients are linearly interpolated from PHOENIX specific intensity stellar models (Husser et al. 2013) for the $1.125 - 1.650 \mu\text{m}$ wavelength range, using the mean values of T_{eff} , $\log g$, and $[\text{Fe}/\text{H}]$ reported in Section 2. Their values are listed in table A.5 and are fixed during the MCMC. Uniform priors are assigned to the systematics model parameters.

For each target, ten chains of 1×10^6 steps each are run for each visit, with 5×10^4 steps for the burn-in. The chains are thinned by a factor ten to reduce correlations among the parameters and their convergence is inspected with the Gelman-Rubin statistics (Gelman & Rubin 1992; Brooks & Gelman 1998). Because of the correlation among the exponential ramp amplitude and time scale, some chains converge to within 3% of unity, instead of a desired 1%. However, the best-likelihood parameters are achieved in a few 10^5 steps at most, for all parameters. In this phase, the two visits of HAT-P-38 b are modeled separately to examine their consistency.

We compare the transit midpoints obtained from our observations, presented in Table 2 to the ground-based observations reported on the ETD database³, as shown in Figure 4. Our findings are consistent with a trend observed since 2011, which suggests the orbital period from Sato et al. (2012) is slightly overestimated. We decide to refine the orbital period by using Sato et al.’s, our observations, and an observation collected on December 27, 2016 (BJD_{TDB} = 2457691.40735669 ± 0.0005) as part of the TRESCA program⁴ because of its good quality. The result, $P = 4.6403294 \pm 0.0000055 \text{ d}$, is 1.6σ lower than Sato et al.’s period and about six times more precise. Figure 4 shows that also the ground-based observations which were not used for the calculation, because of their lower quality (in orange) are consistent with this new period.

Figures 5, 6, and 7 present the raw and corrected band-integrated transits with their respective best-fit models and residuals. We achieve a reduced chi-squared ($\tilde{\chi}^2$) of 1.39 for WASP-67 b. The values $\tilde{\chi}^2 = 1.10$ and $\tilde{\chi}^2 = 1.33$ are obtained for the first and second visit of HAT-P-38 b, respectively. The results are reported in Table 2.

4.2. Spectroscopic transits

The spectroscopic light curves are obtained by integrating the stellar spectrum in channel widths of four to nine pixels (section 3). For each one of such light curves we perform a common-mode correction of the systematics (Stevenson et al. 2014b), that is, each transit is divided by the residuals of the best-likelihood model of the white light curve resulting from the MCMC. The parameter k_r is set as a jump parameter and the transit midpoint t_0 is fixed to the band-integrated light curve best fit. A linear slope is used to model visit-long trends unaccounted for by the white light curve fit. The limb darkening coefficients are interpolated, as previously described, for each spectral channel, and fixed. Their values

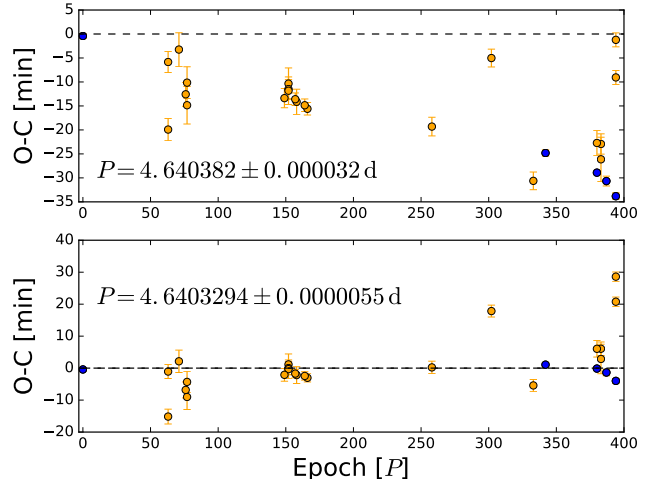


Figure 4. O – C plot for HAT-P-38 b using the orbital period from Sato et al. (2012) (top) and the one calculated with the transits in blue (bottom). The leftmost blue point in both panels corresponds to Sato et al.’s observation. The points in orange were not used for the calculation, due to their lower quality. Non-published values are extracted from the ETD.

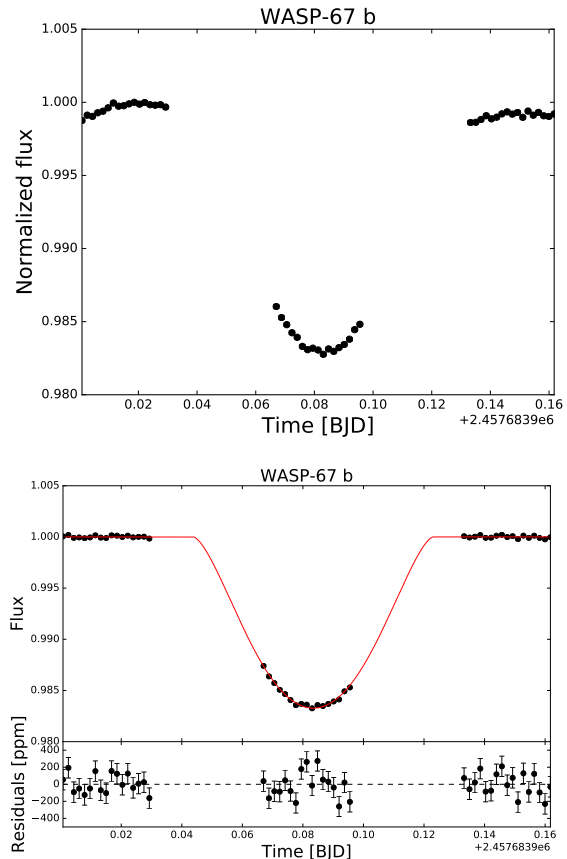


Figure 5. *Top* : Band-integrated transit of WASP-67 b prior to the correction for the systematics. *Bottom* : corrected white light curve (black points) and best-fit model (red curve), after correction for the systematics. The residuals are shown in the lower panels.

are reported in table A.5.

Figures 8 and 9 present the spectroscopic transits after

³ <http://var2.astro.cz/ETD/index.php>

⁴ <http://var2.astro.cz/EN/tresca/>

Table 1

Priors for the transit parameters in the transit fits. $\mathcal{U}(a, b)$ and $\mathcal{J}(a, b)$ denote respectively a uniform and a Jeffreys distribution between a and b .

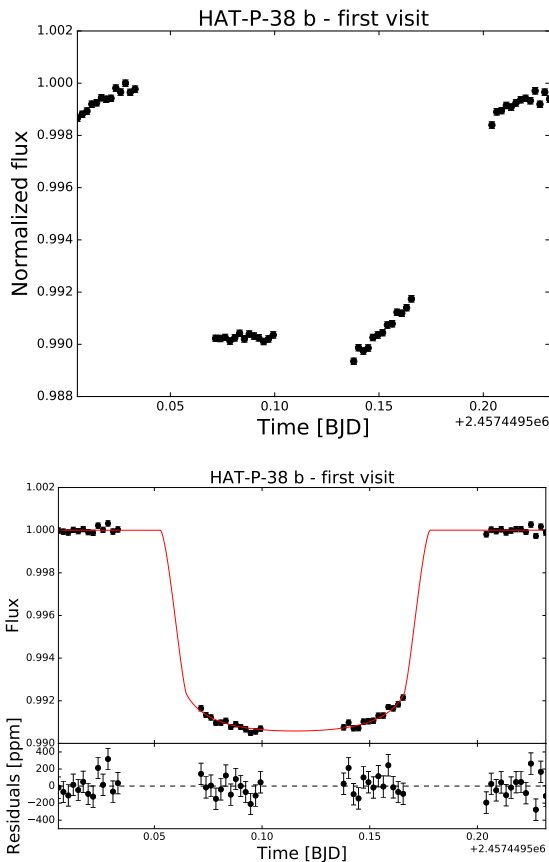
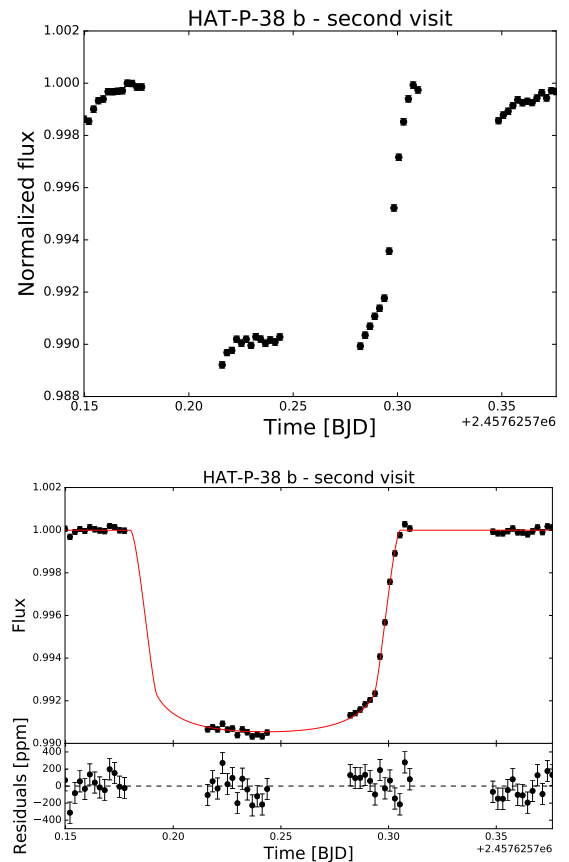
	WASP-67 b	HAT-P-38 b
Radius ratio k_r	$\mathcal{J}(0.07, 0.15)$	$\mathcal{J}(0.07, 0.15)$
Transit midpoint t_0 [BJD] ^(a)	$\mathcal{U}(2457683.40, 2457683.49)$	$\mathcal{U}(2457449.52, 2457449.58)$
Orbital period P [days]	4.61442 (fixed)	4.640382 (fixed)
Normalized semi-major axis a/R_\star ^(a)	12.78 (fixed)	12.18 (fixed)
Orbital inclination i [degrees] ^(b)	85.8 (fixed)	88.3 (fixed)
Orbital eccentricity e	0 (fixed)	0 (fixed)
Limb darkening coefficients u_a, u_b	0.216, 0.220 (fixed)	0.122, 0.319 (fixed)

(^a) Fit on MVRC transit for WASP-67 b: $a/R_\star = 13.5 \pm 0.4$; $i = (85.7 \pm 0.02)^\circ$. (^b) Fit on GPO transit for HAT-P-38 b: $a/R_\star = 11.5 \pm 1.0$; $i = (88.6 \pm 0.04)^\circ$.

Table 2

Results of the MCMC on the white light curves.

	WASP-67 b	HAT-P-38 b - first visit	HAT-P-38 b - second visit
Radius ratio k_r	$0.16066 \pm 2.1 \times 10^{-5}$	$0.09285 \pm 1.9 \times 10^{-4}$	$0.09305 \pm 2.0 \times 10^{-4}$
Transit midpoint t_0 [BJD (TDB)]	$2457683.98419 \pm 0.00013$	$2457450.11375 \pm 0.00045$	$2457626.44542 \pm 0.00010$
Predicted t_0 from ground-based observations, using Sato et al. (2012)'s orbital period [BJD (TDB)]	$2457683.98224 \pm 0.00039$	$2457450.10969 \pm 0.00071$	$2457626.44420 \pm 0.00071$

**Figure 6.** As Figure 5, for the first visit of HAT-P-38 b.**Figure 7.** As Figure 5, for the second visit of HAT-P-38 b.

correction for both the white light curve systematics and the baseline and linear function just described. The fitted transit depths are reported in Tables A.6 and A.7.

A homogeneous reduction of the two visits of HAT-P-

38 b produces two slightly different transmission spectra. The first visit presents a slope in the spectrum of unidentified origin, which significantly mutes the water absorption feature with respect to the second visit. Despite this, almost all points of the two spectra, considered

independently, agree at 1σ , as shown in Figure 10. The shift of the two visits is more important for $\lambda > 1.55 \mu\text{m}$, as will be later discussed in Section 6.1. The difference between the spectrum of visit 2 and visit 1, where the channels with $\lambda > 1.55 \mu\text{m}$ are excluded, divided by the noise level calculated as the sum of the point-by-point variances, is on average $\simeq 0.6$, therefore not significant. This is consistent with the difference in k_r of the two band-integrated transits, with the noise level calculated in the same way, i.e. $\simeq 0.7$.

The robustness of this difference is verified by varying the background region in the image reduction phase (Section 3), the threshold for the rejection of cosmic rays and bad pixels on the detector, and by repeating the MCMC run with various a/R_* and i , compatibly with the uncertainties reported in literature. Different models for the systematics are also tested (e.g., second-order polynomials for the visit-long trend and polynomial functions; see Wakeford et al. 2016), without solving the difference of the two spectra. Moreover, our residuals do not present indications of red noise that might affect the shape of the transmission spectra. The correlation matrices given by the residuals of the common-mode corrected spectroscopic transits and by their respective models are each compared to correlation matrices representing residuals affected only by white noise (that is, extracted from Gaussian distributions with zero mean and σ equal to the standard deviation of the residuals in each channel). The distance between the correlation matrix of each visit and the white-noise correlation matrix is measured with the metric (Herdin et al. 2005)

$$d_{\text{corr}}(\mathbf{V}, \mathbf{G}) = 1 - \frac{\text{tr}\{\mathbf{V}\mathbf{G}\}}{\|\mathbf{V}\|_f \|\mathbf{G}\|_f} \in [0, 1], \quad (2)$$

where \mathbf{V} and \mathbf{G} are the correlation matrices for the residuals and the one representing white noise, respectively. For f , we use the Frobenius norm (Golub & van Loan 1996). The distance is 0 for matrices equal up to a scaling factor, and 1 for a maximum extent difference. We measure $d_{\text{corr}} < 0.3$ for both visits, with lower values when considering only parts of the matrices (that is, selecting only some channels), and never find any significant difference for the two visits.

We also highlight that the reduced χ^2 of the transit fit on the spectroscopic channels does not provide indications of the presence of red noise. The reduced χ^2 for the two visits are reported in table A.8, which yield $\chi^2 = 1.005 \pm 0.023$ for the first visit and 1.017 ± 0.075 for the second one. We therefore choose to combine the two visits and measure a third spectrum by jointly modeling the two visits in each spectroscopic channel. In the respective MCMC, the radius ratio is shared among the two visits. The resulting combined spectrum is shown as well in Figure 10 and the results of the MCMC are in Table A.7.

5. TRANSMISSION SPECTRA ANALYSIS

5.1. Water absorption significance

In Figure 11, the G141 transmission spectra of WASP-67 b and HAT-P-38 b are compared (see Section 6 for a discussion of the different markers and of the models plotted on the top of the spectra). The significance of

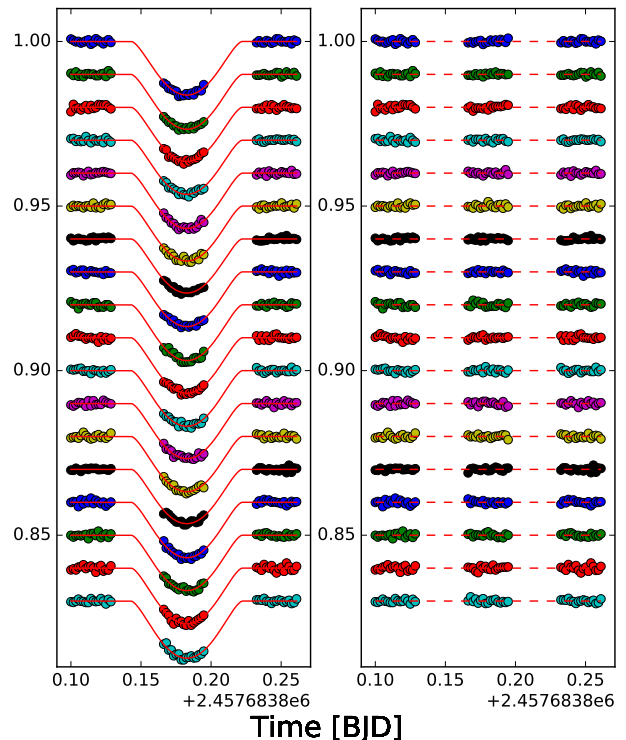


Figure 8. Spectroscopic transits of WASP-67 b after correction for the systematics and best-fit models. Spectrophotometric channels are shifted for clarity. On the right panel, residuals for each transit, shifted to the continuum level of the respective transit.

the spectral features depends on the scale height of each atmosphere.

We use the values in Hellier et al. (2012) for the mass, radius, equilibrium temperature (1040 ± 30 K with zero Bond albedo), and gravity ($g \simeq 5.0 \text{ m s}^{-1}$) in order to derive the scale height H for WASP-67 b. This yields $H = k_B T_{\text{eq}} / (\mu g) \simeq 750$ km, where k_B is Boltzmann’s constant and where we adopt a Jupiter-like mean molecular weight μ (2.3 u). One scale-height change in altitude corresponds to a change in transit depth of

$$D \simeq k_r^2 \sim 2k_r \frac{H}{R_*} \simeq 4 \cdot 10^{-4}. \quad (3)$$

The water absorption amplitude is estimated with the $\text{H}_2\text{O} - \text{J}$ index, following Stevenson (2016). The average transit depth between 1.36 and $1.44 \mu\text{m}$ is used as the measure of the water absorption peak significance. For the J band, i.e. the baseline, we use the 1.22 - $1.24 \mu\text{m}$ wavelength range instead of the one used by Stevenson (1.22 - $1.30 \mu\text{m}$), because of the presence of an absorption feature in that channel. This yields an index of 1.5 ± 0.5 , which indicates the likely presence of obscuring clouds in the atmosphere of WASP-67 b according to Stevenson’s classification.

The same calculation is repeated for the combined visits of HAT-P-38 b, with $T_{\text{eq}} = 1082 \pm 55$ K with zero Bond albedo and $g \simeq 10 \text{ m s}^{-1}$ (Sato et al. 2012). We obtain $H \simeq 420$ km and $D \simeq 1.2 \cdot 10^{-4}$. This implies an $\text{H}_2\text{O} - \text{J}$ index of 1.7 ± 0.9 , suggesting a lower level of muting of spectral features due to condensates.

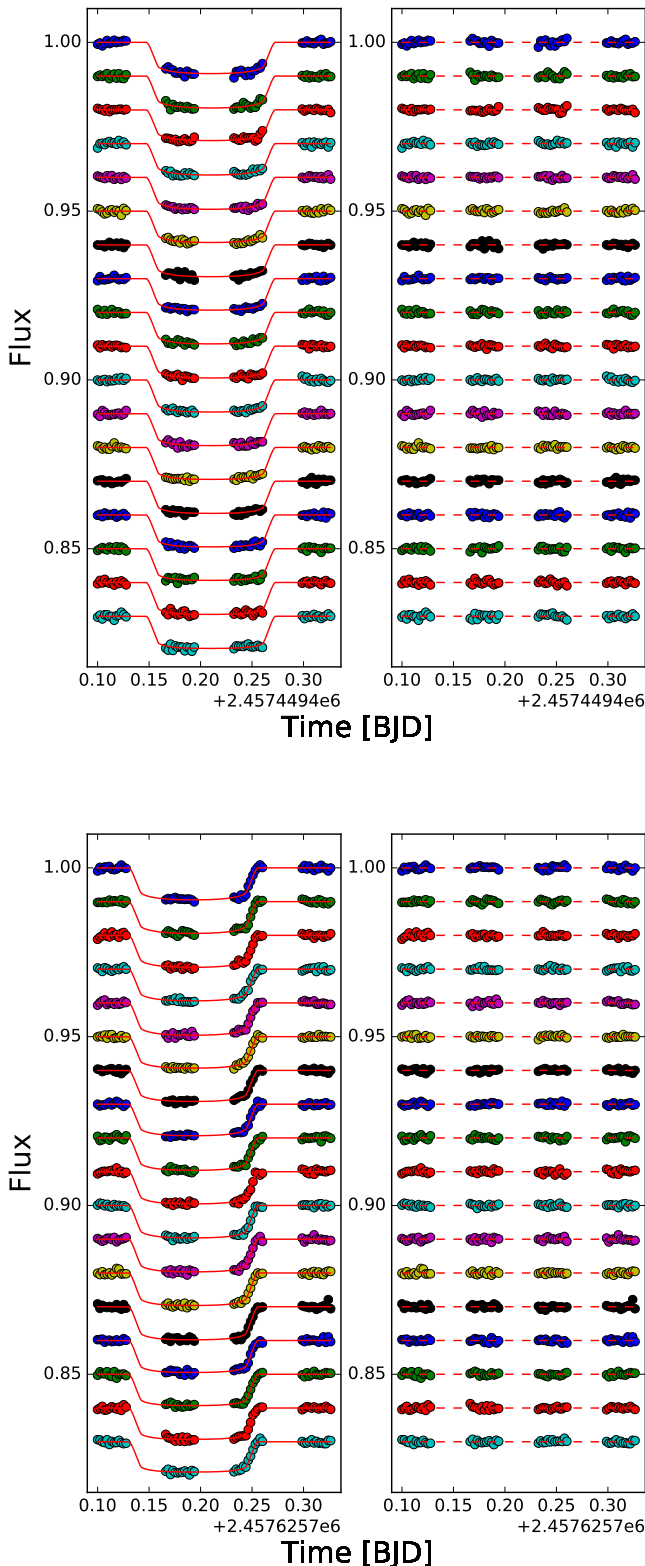


Figure 9. As Figure 8, for HAT-P-38 b. First and second visit on top and bottom panel, respectively.

Given the uncertainties on the indexes, we refrain from giving any interpretation on their values, in particu-

lar with reference to the trends observed by Stevenson (2016). The large error bars are due to the uncertainties on the measured transit depths and an additional level of uncertainty on the cloudiness of these atmospheres is given by the cloud top pressure–metallicity degeneracy (e.g. Seager & Sasselov 2000; Charbonneau et al. 2002; Fortney 2005; Benneke & Seager 2012; Sing et al. 2016), which Stevenson’s index cannot capture. We explore the degeneracy in more detail with retrieval exercises, described below.

6. RETRIEVALS

We use retrievals to explore the molecular abundances, atmospheric temperature, and cloud top pressure allowed for by observations (e.g. Benneke & Seager 2012; Line et al. 2013; Kreidberg et al. 2015). Our retrievals are performed with the CHIMERA suite (Line et al. 2013), which uses the nested Bayesian sampler PyMultiNest to derive the posterior distributions of the model parameters (Feroz et al. 2009; Buchner et al. 2014). In its formalism, a transmission spectrum is described by three parameters determining the P-T structure of the atmosphere (irradiation temperature T_{irr} , IR opacity $\log \kappa_{\text{IR}}$, ratio of visible to IR opacity $\log \gamma_1$), two determining global and relative abundances (metallicity $\log[M/H]$ and carbon-to-oxygen abundance ratio $\log(C/O)$), two accounting for disequilibrium processes through the vertical quench pressures for carbon and nitrogen ($\log P_q(C)$ and $\log P_q(N)$), two for the scattering cross section and slope (σ_0 and γ), and one for a gray cloud top pressure ($\log P_c$). A scaling factor for the planetary radius at 10 bar (xR_p) is used to take into account the lack of absolute normalization for the modeled spectrum.

As the available wavelength coverage offers little constraint on the thermal structure of the atmosphere, on the quench pressures, and on scattering, we adopt a nearly isothermal profile by fixing $\log(\kappa_{\text{IR}})$ and $\log \gamma_1$. As the data encodes no information on quenching processes, we turn off quenching by setting the quench pressures to the μbar value. Finally, as scattering does not contribute to spectral features in the near IR, we impose no scattering by fixing a negligible scattering cross section and setting $\gamma = -4$. We adopt uniform priors for all the other parameters, as listed in table 3.

We perform at first a retrieval with the assumption of chemical equilibrium. Retrievals where this assumption is relaxed are presented, too. In these latter, metallicity and C/O ratio are fixed to their solar values ($[M/H] = 0.0$ and -0.26 , respectively), while water and methane abundances are free parameters and do not scale with the abundances of the other modeled molecules.

6.1. The two visits of HAT-P-38 b

Because of the difference in the visits of HAT-P-38 b, exploration retrievals are at first performed for each visit, separately. The results are presented in Figure 12, top panel, where the retrieved water abundances are shown for the first and second visit and for the combined transmission spectrum. The high-abundance parts of the distributions, on the right of the vertical dashed line at $\log \text{H}_2\text{O} = -2$, imply a $\gtrsim 100\times$ solar metallicity, hard to explain given current giant planet composition models (e.g. Thorngren et al. 2016).

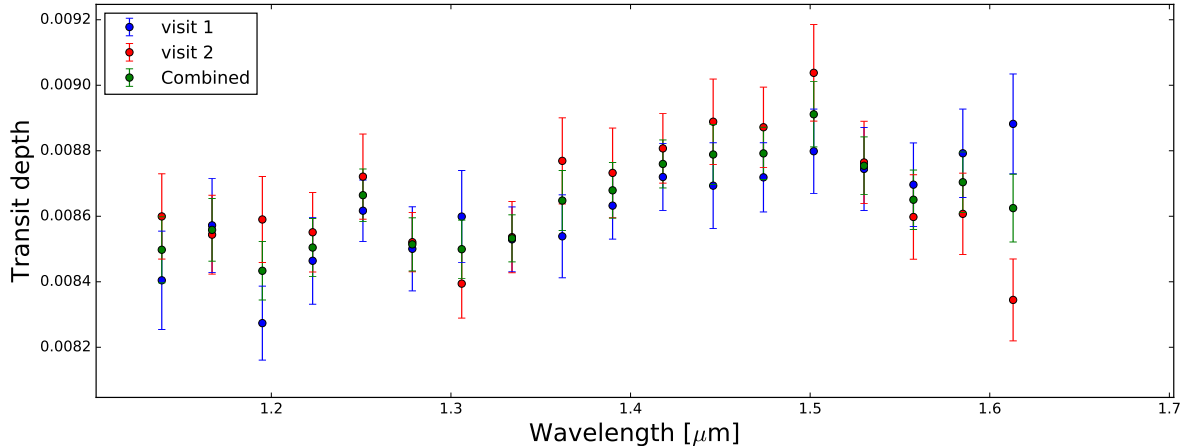


Figure 10. Transmission spectra for the first and second visit of HAT-P-38 b, and from the joint modeling of the two visits.

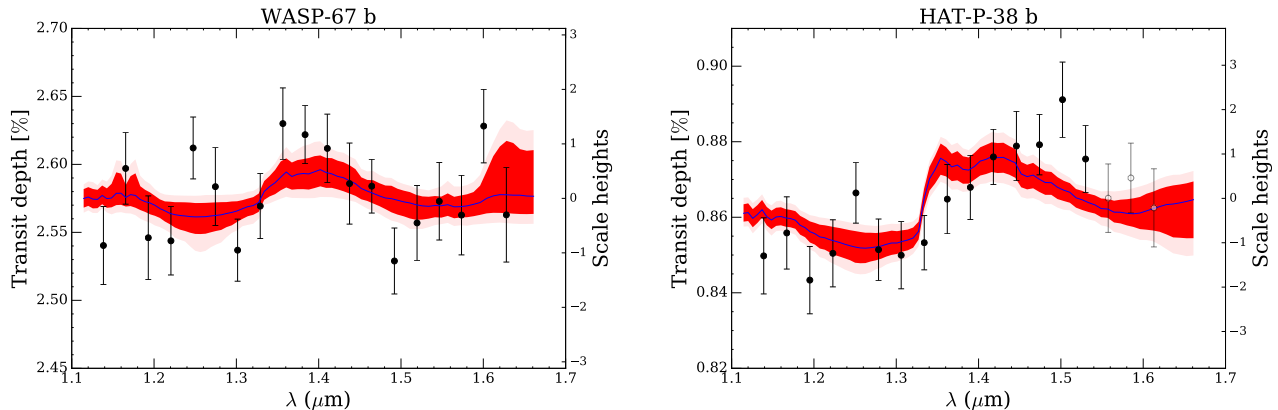


Figure 11. Best-likelihood solution (blue), 1- and 2 σ (shades of red) confidence regions for the retrieved models on WASP-67 b data (*left*) and HAT-P-38 b data (*right*). The empty circles for HAT-P-38 b correspond to the points which are rejected for the retrievals (Section 6.1). The atmospheric scale heights corresponding to the spectral features are on the right of each plot.

Lower abundances are at about 3σ agreement for the two visits. The low-abundance part of the posterior distribution for the combined visit lies in between the two individual visits, while the high-abundance part of this posterior distribution is more peaked than the two visits taken individually. Moreover, the posterior distributions for T_{irr} , shown in Figure 12, central panel, show that the retrievals for the first visit and for the combined spectrum move towards too high temperatures, given the $T_{\text{eq}} \sim 1080$ K found by Hellier et al. (2012). To find the peak of the T_{irr} posterior distribution of the combined spectrum, it is necessary to broaden the uniform distribution prior in Table 3 from 800 to 2000 K. The average value of the posterior is ~ 1800 K. The complete posterior distribution for the combined spectrum, together with the related 15.9%, 50%, and 84.1% percentiles, are shown for clarity in a separate panel (lowest in the Figure).

The difference in the water abundances and the too high T_{irr} are driven by the redder channels of the two visits. To test this, we cut the two transmission spectra at wavelengths larger than $1.55 \mu\text{m}$ and repeat the separate retrievals. As shown in Figure 13, the water abundances are now in agreement.

Following this comparison and because we find no indi-

cation of red noise or instrumental artifacts affecting any of the two visits (section 4.2), we choose to analyze the combined spectrum from which the wavelengths larger than $1.55 \mu\text{m}$ are removed. In the following sections, the complete retrievals for this latter spectrum are presented.

6.2. With chemical equilibrium

The reduced χ^2 , log-likelihood and Bayesian Information Criterion (BIC) of the best-fit model from the retrieval are reported in Table 4. The best likelihood solutions and the 1- and 2 σ confidence regions from the retrievals are overplotted to the spectra of each target in Figure 11. In the panel presenting HAT-P-38 b, the points at wavelength larger than $1.55 \mu\text{m}$ are not considered in the retrieval, as discussed in Section 6.1. In Figure 14, the marginalized posterior distributions and correlation plots for both targets are shown.

The posterior distributions are driven by the muted absorption features. For the two targets, the posteriors for T_{irr} are in agreement at the 1σ level, even if slightly colder solutions are preferred for WASP-67 b. Colder solutions correspond to lower scale heights, which allow to fit for weaker absorption features. No particular physical meaning has to be attributed to these results.

Bimodal posterior distributions for $[M/H]$ are found

Table 3

Priors for the retrievals. $\mathcal{U}(a, b)$ denotes a uniform distribution between a and b .

T_{irr} [K]	$\mathcal{U}(800, 1300)$
$\log(\kappa_{\text{IR}})$ [cm^2g^{-1}]	0.03 (fixed)
$\log \gamma_1$	1 (fixed)
[Fe/H] [\times solar] ^(a)	$\mathcal{U}(10^{-4}, 10^3)$
$\log(C/O)$ ^(b)	$\mathcal{U}(-2, 2)$
Quench pressure $P_q(C)$ [log bar]	-6 (fixed)
Quench pressure $P_q(N)$ [log bar]	-6 (fixed)
Rayleigh Haze σ_0 [σ_{H_2}]	0 (fixed)
Rayleigh Haze γ	-4 (fixed)
Cloud P_c [log bar]	$\mathcal{U}(-7, 2.5)$
R_p scaling factor	$\mathcal{U}(0.5, 1.5)$
H_2O abundance [log mixing ratio] ^(c)	$\mathcal{U}(-12, 0)$
CH_4 abundance [log mixing ratio] ^(c)	$\mathcal{U}(-12, 0)$

(^a) Jump parameter for the retrieval under the assumption of chemical equilibrium; fixed to solar otherwise. (^b) Jump parameter for the retrieval under the assumption of chemical equilibrium; fixed to solar (-0.26) otherwise. (^c) Jump parameter for the retrieval without the assumption of chemical equilibrium; fixed to 0 (in log units) otherwise.

Table 4

Reduced χ^2 , log-likelihood and BIC of the best-fit retrieved atmospheric models.

	Chemical equilibrium	Free abundances
WASP-67 b		
$\bar{\chi}^2$	1.72	1.62
$\ln \mathcal{L}$	-7.44	-7.02
BIC	28.73	27.91
HAT-P-38 b		
$\bar{\chi}^2$	2.02	1.99
$\ln \mathcal{L}$	-8.73	-8.74
BIC	31.00	31.01

for both targets. The two modes separate a region with $[\text{M}/\text{H}] \gtrsim 30\times$ (higher mean molecular weight) and $\lesssim 30\times$ (lower mean molecular weight) solar metallicity. The low-mean molecular weight solutions are favored by our understanding of giant planets composition (e.g. Thorngren et al. 2016), where the retrievals recover the $[\text{M}/\text{H}]-P_c$ degeneracy. For such solutions, we observe mainly $\sim 0.01-10\times$ solar solutions for WASP-67 b and the placement of a cloud deck at higher altitude for WASP-67 b ($\gtrsim 1$ mbar at 1σ) than for HAT-P-38 b ($\gtrsim 150$ mbar at 1σ).

As expected, WFC3 observations do not constrain the C/O ratios. High values of C/O ratios are allowed for by WASP-67 b. This is due to the point at $1.6 \mu\text{m}$ in the spectrum, which is however isolated. The transit depth at this particular wavelength is found to be dependent on the binning during the reduction (section 3) and we therefore warn it has to be considered with caution. We finally remark the correlation between the physical retrieved parameters and the scaling of the planetary radius, reflecting the uncertainty of the reference pressure for the computation of the spectrum. In addition, the scaling of the planetary radius and the cloud top pressure are correlated, as a variation in the pressure where the optical depth goes to zero can be compensated by changing the reference radius for the planet (e.g. Lecavelier Des Etangs et al. 2008; Heng & Kitzmann 2017).

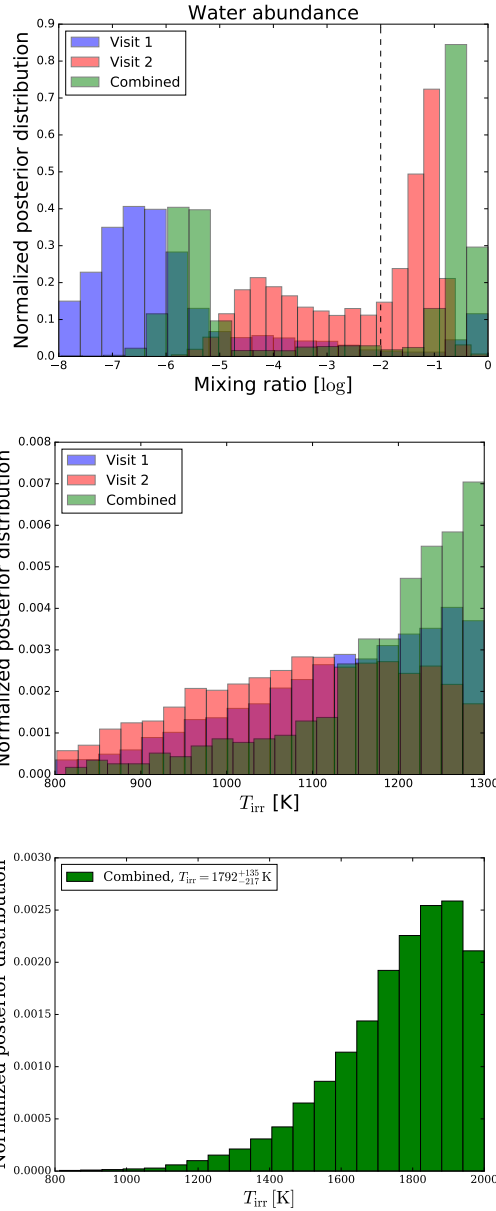


Figure 12. *Top*: Normalized posterior distributions for the water abundance in the first visit (blue), second visit (green) and combined (red) transmission spectrum of HAT-P-38 b. The vertical dashed lines separates the low-metallicity mode (mixing ratio $< 10^{-2}$) from the high-metallicity one (mixing ratio $> 10^{-2}$), as discussed in Section 6.1. *Center*: Marginalized posterior distribution for the T_{irr} on the combined spectrum of HAT-P-38 b, with no point rejected, and with a prior on T_{irr} going from 800 to 2000 K. The posterior for the combined spectrum is cut at the same value of the separate visits priors for clarity. *Bottom*: Complete marginalized posterior distribution for T_{irr} on the combined spectrum of HAT-P-38 b, with no point rejected, together with the 15.9%, 50%, and 84.1% percentiles.

6.3. Without chemical equilibrium

The reduced χ^2 , log-likelihood and BIC of the best-fit model from this retrieval are reported in Table 4. As the best-likelihood models are indistinguishable by eye from the previous retrievals, we refer to Figure 11 for the best-likelihood models and confidence regions. Relaxing the requirement of chemical equilibrium by fixing the metallicity and C/O ratio to solar values ($[\text{M}/\text{H}] =$

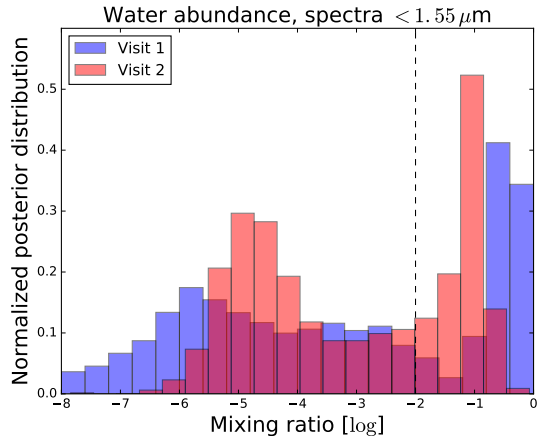


Figure 13. Normalized posterior distribution for the two visits, where the part of the spectra with $\lambda > 1.55\mu\text{m}$ was removed. The black dashed lines separates the two modes found by the retrievals. Abundances larger than $\log 2$ are difficult to explain given our knowledge of Jupiter-like exoplanets.

0, $C/O = -0.26$) enables retrieving the abundances of water and methane. Plot 15 shows the marginalized posterior distributions and correlation plots for the retrieved parameters.

The water abundance for both targets shows a bimodal distribution, which confirms the bimodal posteriors retrieved for the metallicity. Strong correlations are found between the cloud top pressure and the water abundance in the low-abundance mode, as for the metallicity. Solar and sub-solar water abundances are retrieved for both targets, with lower abundances allowed for WASP-67 b than for HAT-P-38 b (mixing ratio $\gtrsim 3 \times 10^{-7}$ against $\gtrsim 2 \times 10^{-6}$ at 1σ ; the solar water abundance corresponds to $\sim 10^{-4}$, Lodders et al. 2009). High water abundance solutions, corresponding to the high-metallicity solutions of the retrieval with chemical equilibrium, are retrieved for HAT-P-38 b. Such solutions correspond to implausibly water-rich atmospheres, which would be hardly compatible with current models of giant planet composition. However, as these solutions are allowed for by the observations, they are conservatively reported.

Large uncertainties for the methane abundance are retrieved in both cases. As expected, given the point at about $1.6\mu\text{m}$ already discussed for WASP-67 b, the uncertainty for methane is larger for this target. Over all, our abundances are in agreement with those found by Tsiaras et al. (2017), who performed retrievals on a large number of planets and allowed mixing ratios down to 10^{-10} . As Tsiaras et al. present only one spectrum per HAT-P-38 b, however, we are not able to conclude whether they also find the same difference between the two visits.

7. DISCUSSION

The measured spectra of WASP-67 b and HAT-P-38 b indicate that these twin planets, with nearly identical temperatures, gravities, and host stars, have very different atmospheric properties. Indeed, atmospheric metallicity is another unavoidable parameter to consider, in order to determine the composition of clouds which can affect a transmission spectrum (Visscher et al. 2006, 2010; Morley et al. 2015). First-order expectations on the condensed species are usually obtained from atmospheric

models with solar composition. In this scenario, the P-T structure of the atmosphere is compared to Clausius-Clapeyron curves for the dominant species, determining e.g. the base pressure and extent of clouds (Sánchez-Lavega et al. 2004).

Focusing on two planets with nearly equal temperature and gravity, we can isolate the role of metallicity in shaping transmission spectra. From current constraints of the planet mass-metallicity relation (e.g. Wakeford et al. 2017a, and references therein), we expect both HAT-P-38 b and WASP-67 b to lie in a metallicity range of $1 \times$ to $10 \times$ solar. Given the smaller mass of HAT-P-38 b with respect to WASP-67 b (0.27 against $0.42 M_J$), we also expect the former to be slightly more metal-rich than the latter. A higher metallicity for HAT-P-38 b than for WASP-67 b would cause a shift of both the P-T profiles of Figure 1 and of the condensation curves on the temperature axis, as shown in Figure 16. As a result, alkali-bearing condensates such as MnS and Na_2S would form deeper in the atmosphere for WASP-67 b than for HAT-P-38 b, obscuring to a larger extent the pressure regime probed by transmission spectroscopy. The comparison of these two planets points, therefore, to the possibility of constraining the composition of exoplanet atmospheres by using the muting of spectral features due to aerosols.

Current observations in the near-infrared, however, cannot effectively constrain $[M/H]$ nor cloud species. Retrievals rely on a generic gray cloud top pressure and the role of metallicity in shaping transmission spectra cannot be clearly elucidated. Advances in this direction need a broader wavelength coverage. Optical wavelengths are already accessible by present instrumentation and allow constraining the kind of atmospheric aerosols, especially hazes. *HST*/*STIS* would be particularly suitable for distinguishing different scattering particle sizes and slopes (e.g. Lecavelier Des Etangs et al. 2008), in order to constrain the scattering parameters σ_0 and γ which do not affect G141 observations. By probing alkali lines, observations in the visible would also constrain the temperature structure of the atmospheres above 1 mbar (e.g. Vidal-Madjar et al. 2011a,b), complementing near-IR observations which can only probe regions between $\sim 1 - 100$ mbar. A better constraint on the P-T profiles would allow more detailed retrievals on the atmospheric parameters, relaxing the assumption of nearly isothermal atmosphere, and a better insight on the base pressure of the cloud species.

The mid-IR ($5 - 28\mu\text{m}$) is another spectral region of crucial interest. Observations in this band would allow the distinction of condensates vibrational modes and therefore of different condensate species (Wakeford & Sing 2015). *JWST*/*MIRI* will be able to shed light on this aspect.

Giant planets are expected to retain much of their primordial composition after their formation and evolution. The abundances we observe are therefore the result of the composition of the protoplanetary disk where they formed, of their initial location in the disk, and of the accreted materials during the evolution history (e.g. Pollack et al. 1996; Boss 1997; Alibert et al. 2005; Madhusudhan et al. 2011; Helling et al. 2014; Kreidberg et al. 2014a; Mordasini et al. 2016; Thorngren et al. 2016, and references therein). The different characteristics of the

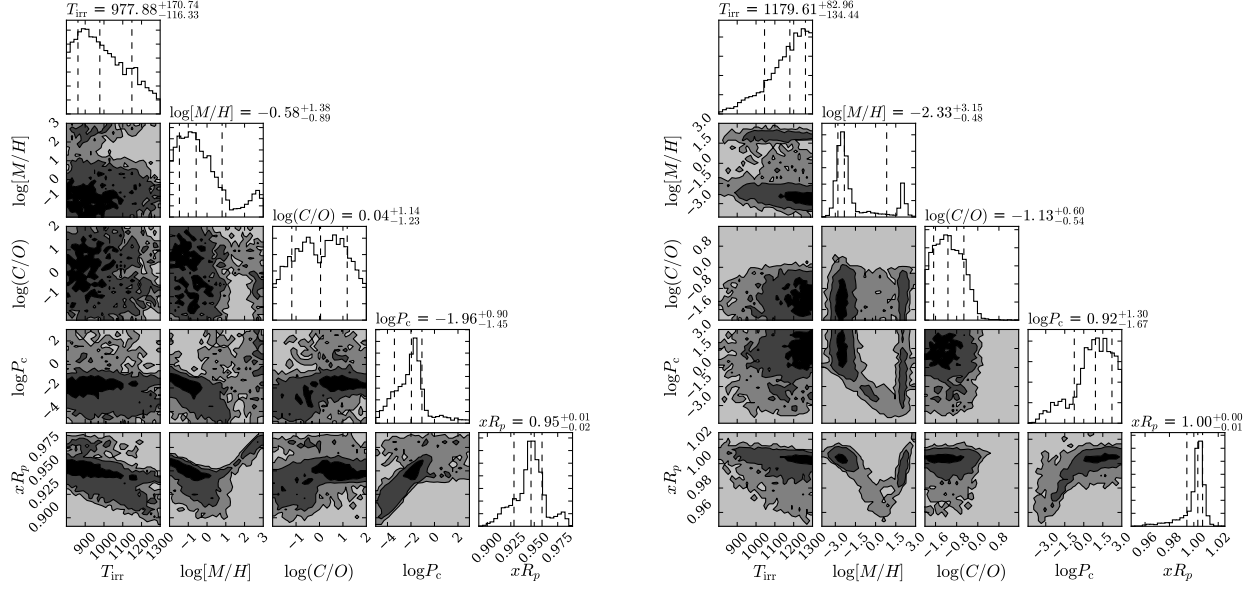


Figure 14. Marginalized posterior distributions and correlation plots resulting from the retrieval on WASP-67 b (left) and HAT-P-38 b (right) assuming chemical equilibrium. Above each histogram, the 15.9%, 50%, and 84.1% percentiles are reported.

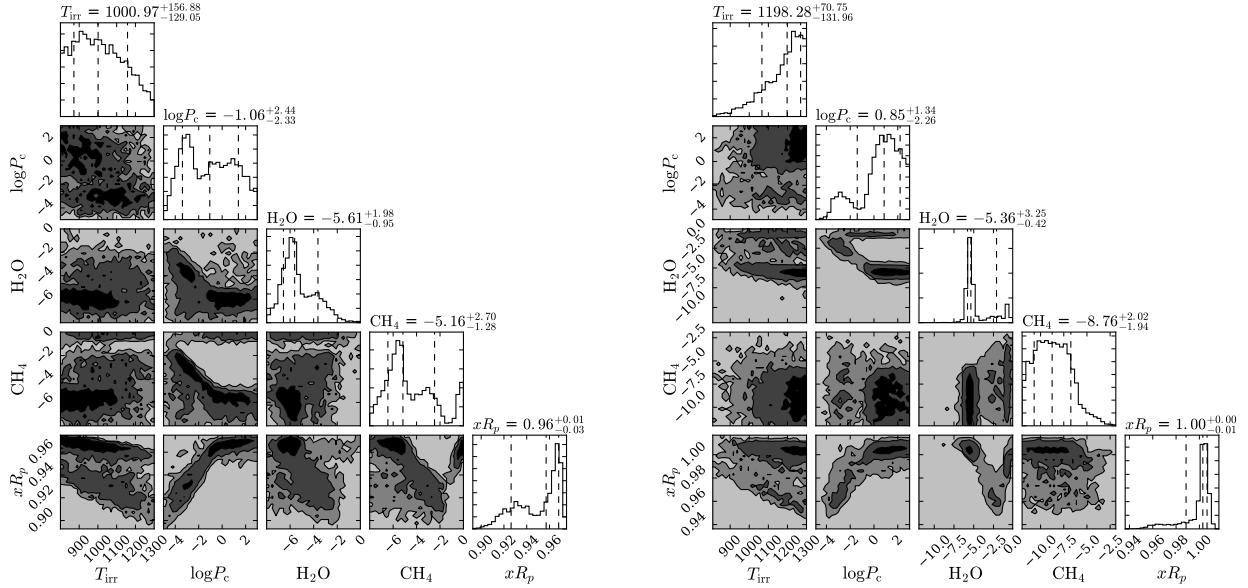


Figure 15. Marginalized posterior distributions and correlation plots resulting from the retrieval on WASP-67 b (left) and HAT-P-38 b (right) without assuming chemical equilibrium. Percentiles are reported as in Figure 14.

two atmospheres keep trace of their different formation and evolution environments. In this context, the measurement of the scattering signature in the visible with STIS would enable breaking the cloud-metallicity degeneracy in the retrievals (e.g. Benneke & Seager 2012), improving our knowledge of the mass-metallicity relation for giant planets. The resulting constraints on their formation and evolutionary history are particularly valuable for HAT-P-38 b, as little sampling is currently available for Saturn-mass bodies.

Population synthesis models which follow the entire planets' history and return their composition at the end

of their migration were explored in few studies, and strong observational constraints on the outcome of the models are expected with instruments such as JWST and the ESA candidate mission ARIEL (Pace et al. 2016). This is one more reason to pursue follow-up observations in both visible and mid-IR of WASP-67 b and HAT-P-38 b, in order to access vital information for planet evolutionary models.

We remark in this place the importance of compared analysis. Similar reductions of the spectra and light curve fits were performed independently by different members of our team. The comparison of the results

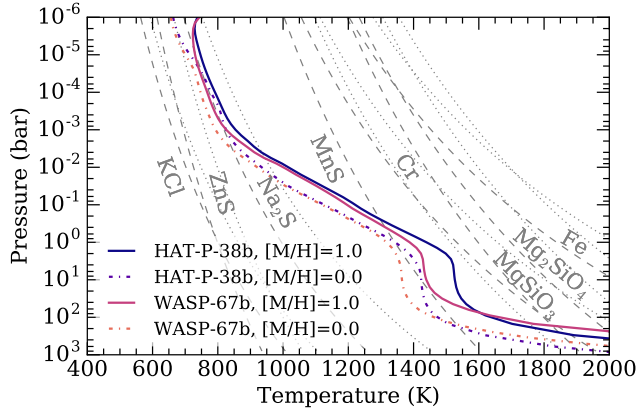


Figure 16. Difference in the P-T profiles of WASP-67 b and HAT-P-38 b from $1\times$ (dashed lines) to $10\times$ (continuous lines) solar metallicity. Given the mass-metallicity relation, the P-T profile of WASP-67 b should be closer to the dashed line and the one of HAT-P-38 b closer to the continuous line.

ensured the robustness of the analysis. This was useful both in assessing the importance of the point at $1.6\ \mu\text{m}$ for WASP-67 b and in comparing the two visits of HAT-P-38 b.

8. CONCLUSIONS

We present WFC3/G141 transmission spectroscopy observations of the short-period giant planets WASP-67 b and HAT-P-38 b. While having nearly equal irradiation level ($T_{\text{eq}} \sim 1050\ \text{K}$) and gravity ($g \sim 10\ \text{m s}^{-1}$), thought to be the main parameters determining cloud formation and extent other than composition, the spectra of these two planets are remarkably different.

A slope is observed in the spectrum of the first visit of HAT-P-38 b. Despite the two visits agreeing at 1σ for most channels, the difference in the wavelengths larger than $1.55\ \mu\text{m}$ is large enough to cause unrealistic results in the retrievals on their combined spectrum. Several tests are performed to exclude the presence of red noise in the first visit as in the second. We cannot identify the source of the slope, which we attribute to an instrumental artifact, and we exclude the last channels from our analysis.

The abundances we retrieve for both planets are in agreement with those found by Tsiaras et al. (2017), who perform retrievals large sample of exoplanet spectra. We are unable to conclude whether these authors find a difference in the two visits of HAT-P-38 b, as they present only a spectrum for this planet. We detect water in both planets and attribute the different significance of their water peaks at $1.4\ \mu\text{m}$ both to a muting effect due to obscuring clouds and to different formation and accretion histories. Our analysis also recovers a correlation between the retrieved abundance of water and the cloud base altitude.

Muted water absorption can be explained by sub-solar water abundance, solar water abundance with clouds, or very high water abundance. Given the masses of these planets, however, both very low and very high metallicity solutions are disfavored. For the solar and sub-solar abundance, we recover the cloud top-pressure-metallicity degeneracy. We suggest that the different atmospheric metallicity of the planets, likely separated by

about an order of magnitude, affects the base pressure of alkali clouds, as expected from aerosol models in literature. As G141, near-IR observations alone are not able to constrain metallicity nor cloud top pressure, optical (*HST/STIS*) and mid-IR (*JWST* and *ARIEL*) observations are discussed in their potential to solve the degeneracy.

Follow-up observations are particularly important for WASP-67 b and HAT-P-38 b, as their comparative study could unveil vital information for the understanding of aerosols in giant planet atmospheres.

Based on observations made with the NASA/ESA Hubble Space Telescope, obtained from the data archive at the Space Telescope Science Institute. STScI is operated by the Association of Universities for Research in Astronomy, Inc. under NASA contract NAS 5-26555. These observations are associated with program GO 14260.

Facilities: *HST*(WFC3).

REFERENCES

- Alibert, Y., Mordasini, C., Benz, W., & Winisdoerffer, C. 2005, *A&A*, 434, 343
- Baker, S., & Matthews, I. 2001, Proceedings of the 2001 IEEE Conference on Computer Vision and Pattern Recognition, Volume 1, Pages 1090–1097
- Benneke, B., & Seager, S. 2012, *ApJ*, 753, 100
- Berta, Z. K., Charbonneau, D., Désert, J.-M., et al. 2012, *ApJ*, 747, 35
- Boss, A. P. 1997, *Science*, 276, 1836
- Brooks, S. P., & Gelman, A. 1998, *Journal of Computational and Graphical Statistics*, 7, 434
- Buchner, J., Georgakakis, A., Nandra, K., et al. 2014, *A&A*, 564, A125
- Burrows, A., Marley, M. S., & Sharp, C. M. 2000, *ApJ*, 531, 438
- Charbonneau, D., Brown, T. M., Noyes, R. W., & Gilliland, R. L. 2002, *ApJ*, 568, 377
- Claret, A. 2000, *A&A*, 363, 1081
- Cubillos, P., Harrington, J., Lust, N., et al. 2016, MC3: Multi-core Markov-chain Monte Carlo code, *Astrophysics Source Code Library*, ascl:1610.013
- Deming, D., Wilkins, A., McCullough, P., et al. 2013, *ApJ*, 774, 95
- Doyle, L. R., Carter, J. A., Fabrycky, D. C., et al. 2011, *Science*, 333, 1602
- Enoch, B., Cameron, A. C., Anderson, D. R., et al. 2011, *MNRAS*, 410, 1631
- Feroz, F., Hobson, M. P., & Bridges, M. 2009, *MNRAS*, 398, 1601
- Fortney, J. J. 2005, *MNRAS*, 364, 649
- Fortney, J. J., Lodders, K., Marley, M. S., & Freedman, R. S. 2008, *ApJ*, 678, 1419
- Fortney, J. J., Marley, M. S., & Barnes, J. W. 2007, *ApJ*, 659, 1661
- Fortney, J. J., Sudarsky, D., Hubeny, I., et al. 2003, *ApJ*, 589, 615
- Fraine, J., Deming, D., Benneke, B., et al. 2014, *Nature*, 513, 526
- Gelman, A., & Rubin, D. B. 1992, *Statist. Sci.*, 7, 457
- Golub, G. H., & van Loan, C. F. 1996, *Matrix computations*
- Gregory, P. C. 2005, *Bayesian Logical Data Analysis for the Physical Sciences: A Comparative Approach with ‘Mathematica’ Support* (Cambridge University Press)
- Hartman, J. D., Bakos, G. Á., Sato, B., et al. 2011, *ApJ*, 726, 52
- Hellier, C., Anderson, D. R., Collier Cameron, A., et al. 2012, *MNRAS*, 426, 739
- Helling, C., Woitke, P., Rimmer, P. B., et al. 2014, *Life*, 4, arXiv:1403.4420
- Heng, K., & Kitzmann, D. 2017, *ArXiv e-prints*, arXiv:1702.02051
- Herdin, M., Czink, N., Özcelik, H., & Bonek, E. 2005
- Horne, K. 1986, *PASP*, 98, 609
- Husser, T.-O., Wende-von Berg, S., Dreizler, S., et al. 2013, *A&A*, 553, A6
- Kilpatrick, B. M., Cubillos, P. E., Stevenson, K. B., et al. 2017, *ArXiv e-prints*, arXiv:1704.07421

- Knutson, H. A., Dragomir, D., Kreidberg, L., et al. 2014, *ApJ*, 794, 155
- Kreidberg, L., Bean, J. L., Désert, J.-M., et al. 2014a, *ApJL*, 793, L27
- . 2014b, *Nature*, 505, 69
- Kreidberg, L., Line, M. R., Bean, J. L., et al. 2015, *ApJ*, 814, 66
- Lecavelier Des Etangs, A., Pont, F., Vidal-Madjar, A., & Sing, D. 2008, *A&A*, 481, L83
- Line, M. R., Wolf, A. S., Zhang, X., et al. 2013, *ApJ*, 775, 137
- Lodders, K. 1999, *ApJ*, 519, 793
- Lodders, K., Palme, H., & Gail, H.-P. 2009, *Landolt Börnstein*, arXiv:0901.1149
- Madhusudhan, N., Amin, M. A., & Kennedy, G. M. 2014a, *ApJL*, 794, L12
- Madhusudhan, N., Crouzet, N., McCullough, P. R., Deming, D., & Hedges, C. 2014b, *ApJL*, 791, L9
- Madhusudhan, N., Mousis, O., Johnson, T. V., & Lunine, J. I. 2011, *ApJ*, 743, 191
- Mancini, L., Southworth, J., Ciceri, S., et al. 2014, *A&A*, 568, A127
- Mandel, K., & Agol, E. 2002, *ApJL*, 580, L171
- Marley, M. S., Saumon, D., Guillot, T., et al. 1996, *Science*, 272, 1919
- McCullough, P., & MacKenty, J. 2012, *Considerations for using Spatial Scans with WFC3*, Tech. rep.
- McKay, C. P., Pollack, J. B., & Courtin, R. 1989, *Icarus*, 80, 23
- Mordasini, C., van Boekel, R., Mollière, P., Henning, T., & Benneke, B. 2016, *ApJ*, 832, 41
- Morley, C. V., Fortney, J. J., Marley, M. S., et al. 2012, *ApJ*, 756, 172
- . 2015, *ApJ*, 815, 110
- Pace, E., Micela, G., & Ariel Team. 2016, *Mem. Soc. Astron. Italiana*, 87, 214
- Parviainen, H. 2015, *MNRAS*, 450, 3233
- Pirzkal, N., Ryan, R., & Brammer, G. 2016, *Trace and Wavelength Calibrations of the WFC3 G102 and G141 IR Grisms*, Tech. rep.
- Pollack, J. B., Hubickyj, O., Bodenheimer, P., et al. 1996, *Icarus*, 124, 62
- Sánchez-Lavega, A., Pérez-Hoyos, S., & Hueso, R. 2004, *American Journal of Physics*, 72, 767
- Sato, B., Hartman, J. D., Bakos, G. Á., et al. 2012, *PASJ*, 64, 97
- Seager, S., Richardson, L. J., Hansen, B. M. S., et al. 2005, *ApJ*, 632, 1122
- Seager, S., & Sasselov, D. D. 2000, *ApJ*, 537, 916
- Sing, D. K., Fortney, J. J., Nikolov, N., et al. 2016, *Nature*, 529, 59
- Stevenson, K. B. 2016, *ApJL*, 817, L16
- Stevenson, K. B., Bean, J. L., Fabrycky, D., & Kreidberg, L. 2014a, *ApJ*, 796, 32
- Stevenson, K. B., Bean, J. L., Seifahrt, A., et al. 2014b, *AJ*, 147, 161
- Sudarsky, D., Burrows, A., & Hubeny, I. 2003, *ApJ*, 588, 1121
- Thorngren, D. P., Fortney, J. J., Murray-Clay, R. A., & Lopez, E. D. 2016, *ApJ*, 831, 64
- Tsiaras, A., Waldmann, I. P., Zingales, T., et al. 2017, *ArXiv e-prints*, arXiv:1704.05413
- Vidal-Madjar, A., Sing, D. K., Lecavelier Des Etangs, A., et al. 2011a, *A&A*, 527, A110
- Vidal-Madjar, A., Huitson, C. M., Lecavelier Des Etangs, A., et al. 2011b, *A&A*, 533, C4
- Visser, C., Lodders, K., & Fegley, Jr., B. 2006, *ApJ*, 648, 1181
- . 2010, *ApJ*, 716, 1060
- Wakeford, H. R., & Sing, D. K. 2015, *A&A*, 573, A122
- Wakeford, H. R., Sing, D. K., Evans, T., Deming, D., & Mandell, A. 2016, *ApJ*, 819, 10
- Wakeford, H. R., Sing, D. K., Kataria, T., et al. 2017a, *Science*, 356, 628
- Wakeford, H. R., Stevenson, K. B., Lewis, N. K., et al. 2017b, *ApJL*, 835, L12

APPENDIX

ADDITIONAL FIGURES AND TABLES

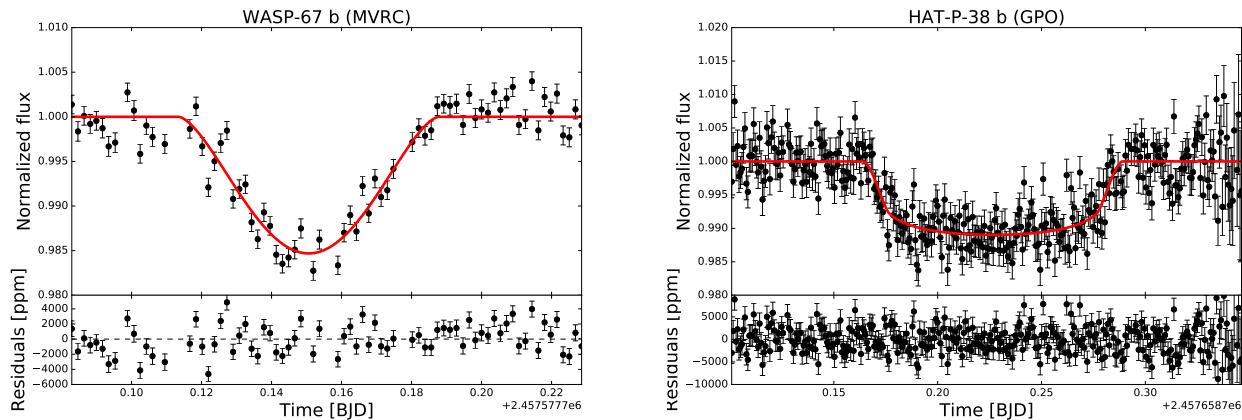


Figure A.17. MVRC observations of the transit of WASP-67 b (*left*) and GPO observation of the transit of HAT-P-38 b (*right*), with their respective best-likelihood fits.

Table A.5

Limb darkening coefficients for WASP-67 (left) and HAT-P-38 (right). The first column of each table indicates the wavelength range corresponding to the channel. The second and third columns are for the linear (u_a) and quadratic (u_b) coefficients. For each star, the last row denotes the coefficients for the band-integrated light curve.

λ [μm]	u_a	u_b	λ [μm]	u_a	u_b
1.125-1.157	0.286	0.170	1.125-1.153	0.173	0.288
1.157-1.188	0.274	0.176	1.153-1.181	0.169	0.291
1.188-1.220	0.267	0.182	1.181-1.209	0.162	0.295
1.220-1.252	0.260	0.188	1.209-1.237	0.156	0.298
1.252-1.284	0.244	0.203	1.237-1.265	0.151	0.302
1.284-1.315	0.241	0.209	1.265-1.292	0.131	0.312
1.315-1.347	0.230	0.213	1.292-1.320	0.137	0.316
1.347-1.379	0.218	0.226	1.320-1.348	0.129	0.319
1.379-1.410	0.208	0.239	1.348-1.376	0.121	0.324
1.410-1.442	0.199	0.242	1.376-1.404	0.112	0.337
1.442-1.474	0.187	0.250	1.404-1.432	0.108	0.333
1.474-1.506	0.170	0.249	1.432-1.460	0.098	0.338
1.506-1.537	0.152	0.271	1.460-1.488	0.085	0.347
1.537-1.569	0.135	0.274	1.488-1.516	0.080	0.345
1.569-1.601	0.133	0.270	1.516-1.544	0.066	0.353
1.601-1.633	0.119	0.275	1.544-1.571	0.061	0.351
1.125-1.633	0.220	0.218	1.571-1.599	0.058	0.344
			1.599-1.627	0.048	0.346
			1.125-1.627	0.122	0.319

Table A.6

Fitted radius ratio k_r for the spectroscopic transits of WASP-67 b. The left column corresponds to the central wavelength of each spectral channel.

λ [μm]	WASP-67 b
1.172	0.16035 ± 0.00090
1.204	0.15914 ± 0.00081
1.236	0.16048 ± 0.00064
1.268	0.16125 ± 0.00079
1.300	0.15984 ± 0.00072
1.331	0.16049 ± 0.00067
1.363	0.16181 ± 0.00069
1.394	0.16177 ± 0.00069
1.426	0.16169 ± 0.00072
1.458	0.16054 ± 0.00070
1.490	0.15905 ± 0.00068
1.522	0.15979 ± 0.00076
1.553	0.15985 ± 0.00092
1.585	0.16105 ± 0.00071
1.617	0.16088 ± 0.00086

Table A.7

Fitted radius ratio k_r for the spectroscopic transits of the first (second column), second (third), and combined (fourth) visit of HAT-P-38 b. The leftmost column corresponds to the central wavelength of each spectral channel.

λ [μm]	First visit	Second visit	Combined
1.139	0.09168 ± 0.00082	0.09273 ± 0.00070	0.09218 ± 0.00055
1.167	0.09259 ± 0.00078	0.09243 ± 0.00065	0.09251 ± 0.00052
1.195	0.09096 ± 0.00062	0.09268 ± 0.00071	0.09183 ± 0.00049
1.223	0.09200 ± 0.00072	0.09247 ± 0.00066	0.09222 ± 0.00048
1.251	0.09283 ± 0.00050	0.09339 ± 0.0007	0.09308 ± 0.00043
1.278	0.09220 ± 0.00070	0.09231 ± 0.00049	0.09227 ± 0.00044
1.306	0.09273 ± 0.00076	0.09162 ± 0.00057	0.09219 ± 0.00048
1.334	0.09236 ± 0.00054	0.09239 ± 0.00059	0.09237 ± 0.00039
1.362	0.09241 ± 0.00069	0.09364 ± 0.0007	0.09299 ± 0.00049
1.390	0.09291 ± 0.00055	0.09345 ± 0.00073	0.09316 ± 0.00046
1.418	0.09338 ± 0.00055	0.09385 ± 0.00057	0.09359 ± 0.00039
1.446	0.09324 ± 0.00070	0.09428 ± 0.00069	0.09375 ± 0.00049
1.474	0.09337 ± 0.00057	0.09419 ± 0.00065	0.09377 ± 0.00043
1.502	0.09380 ± 0.00069	0.09507 ± 0.00078	0.0944 ± 0.00053
1.530	0.09351 ± 0.00068	0.09362 ± 0.00067	0.09356 ± 0.00047
1.558	0.09325 ± 0.00068	0.09272 ± 0.00070	0.09301 ± 0.00049
1.585	0.09377 ± 0.00072	0.09278 ± 0.00067	0.0933 ± 0.00049
1.613	0.09424 ± 0.00081	0.09135 ± 0.00068	0.09287 ± 0.00056

Table A.8

Reduced χ^2 for the spectroscopic channels of the two visits of HAT-P-38 b.

λ [μm]	First visit	Second visit
1.153-1.181	0.9996	0.9999
1.125-1.153	0.9998	0.9995
1.181-1.209	0.9996	0.9998
1.209-1.237	1.0000	0.9999
1.237-1.265	0.9997	0.9999
1.265-1.292	0.9997	0.9997
1.292-1.320	0.9999	0.9998
1.320-1.348	0.9997	0.9988
1.348-1.376	0.9997	0.9998
1.376-1.404	0.9998	0.9999
1.404-1.432	0.9998	0.9999
1.432-1.460	0.9998	0.9996
1.460-1.488	0.9996	1.0000
1.488-1.516	0.9997	0.9997
1.516-1.544	0.9999	0.9999
1.544-1.571	0.9997	0.9999
1.571-1.599	0.9999	0.9998
1.599-1.627	0.9998	0.9999